Inorganic Chemistry

Article

pubs.acs.org/IC

Magnetic Structures of $NaFePO_4$ Maricite and Triphylite Polymorphs for Sodium-Ion Batteries

Maxim Avdeev,[†] Zakiah Mohamed,[‡] Chris D. Ling,[‡] Jiechen Lu,[§] Mao Tamaru,[§,∥] Atsuo Yamada,[§,⊥] and Prabeer Barpanda*[§,⊥]

[†]Bragg Institute, B87, Australian Nuclear Science and Technology Organization, Locked Bag 2001, Kirrawee DC NSW 2232, Australia

[‡]School of Chemistry, The University of Sydney, Sydney, NSW 2006, Australia

[§]Department of Chemical System Engineering, The University of Tokyo, 7-3-1 Hongo, Bunkyo-ku, Tokyo 113-8656, Japan

[∥]Mitsubishi Motors Corporation, 1 Nakashinkiri, Hashime-Cho, Okazaki-shi, Aichi 444-8501, Japan

[⊥]Unit of Element Strategy Initiative for Catalysts & Batteries, ESICB, Kyoto University, Kyoto 615-8510, Japan

S *Supporting Information*

ABSTRACT: The magnetic structure and properties of polycrystalline $NaFePO_4$ polymorphs, maricite and triphylite, both derived from the olivine structure type, have been investigated using magnetic susceptibility, heat capacity, and low-temperature neutron powder diffraction. These $NaFePO_4$ polymorphs assume orthorhombic frameworks (space group No. 62, *Pnma*), built from FeO_6 octahedral and PO_4 tetrahedral units having corner-sharing and edge-sharing arrangements. Both polymorphs demonstrate antiferromagnetic ordering below 13 K for maricite and 50 K for triphylite. The magnetic structure and properties are discussed considering super- and supersuperexchange interactions in comparison to those of triphylite-$LiFePO_4$.

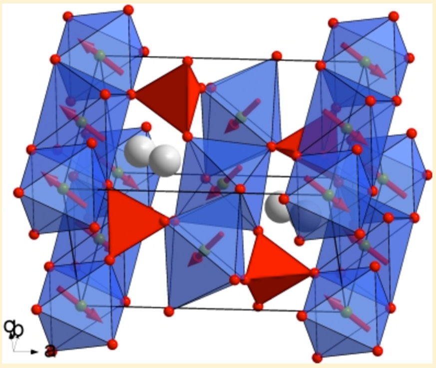

■ INTRODUCTION

Rechargeable Li-ion batteries have grown leaps and bounds over the last two decades since their commercialization by SONY, empowering portable electronics, (plug-in) hybrid electric vehicles, (remote) large-scale grid power storage, and storage devices coupled with renewable energy generators (e.g., solar cells).[1,2] The effort to build better Li-ion batteries has led to the unraveling and optimizing of a wide gamut of oxides as well as polyanionic framework cathode materials.[3,4] While portable electronics and electric vehicle applications focus on the chemistry of Li ions for their small size and energy density, economically viable large-scale applications (e.g., remote grid storage) without any volume restriction may be better served by the chemistry of more abundant Na ions. This has motivated the battery community to explore various oxide and polyanionic cathode materials for sodium-based batteries[5−12] as possible alternatives for their lithium counterparts.[13] Among the polyanionic systems, $LiFePO_4$ has been the flagship cathode candidate.[14−16] This naturally prompts research into its sodium analogue, $NaFePO_4$, as a cathode contender for Na-ion batteries. Unlike $LiFePO_4$, the $NaFePO_4$ analogue exists in two distinct polymorphs (triphylite and maricite). The latter is thermodynamically more stable[17] but built from edge-sharing FeO_6 octahedra with no Na diffusion channel, making it electrochemically inactive.[18] In contrast, the triphylite $NaFePO_4$ polymorph is isostructural to $LiFePO_4$ and offers one-dimensional channels delivering a reversible discharge capacity exceeding 120 mAh/g with an Fe^{3+}/Fe^{2+} redox activity around 3 V.[19,20]

The $LiMPO_4$ family also attracted significant attention due to a remarkable variety of magnetic properties and structures. Originally studied decades ago,[21−23] the compositions with M = Mn−Ni recently received revived interest as systems featuring metal-containing layers weakly magnetically coupled by super-superexchange via phosphate groups and thus demonstrating quasi-2D magnetic behavior.[24−28] The weak interlayer interactions are sensitive to subtle changes in crystal and electronic structure, and depending on the nature of transition metal M the compositions, despite being isostructural, order into different magnetic structures which in turn may be manipulated by high magnetic field.[29−34]

It is noteworthy that although $LiFePO_4$ is often addressed in the literature as “olivine” it should be more accurately described as “triphilite”, since “maricite” is also derived from the olivine structure type. In the aristotype Mg_2SiO_4 olivine structure, Mg atoms occupy two inequivalent sites *M*1(4a) and *M*2(4c) which in phosphates *AM*PO_4 are either occupied by alkali (*A*) and

Received: April 8, 2013
Published: July 11, 2013

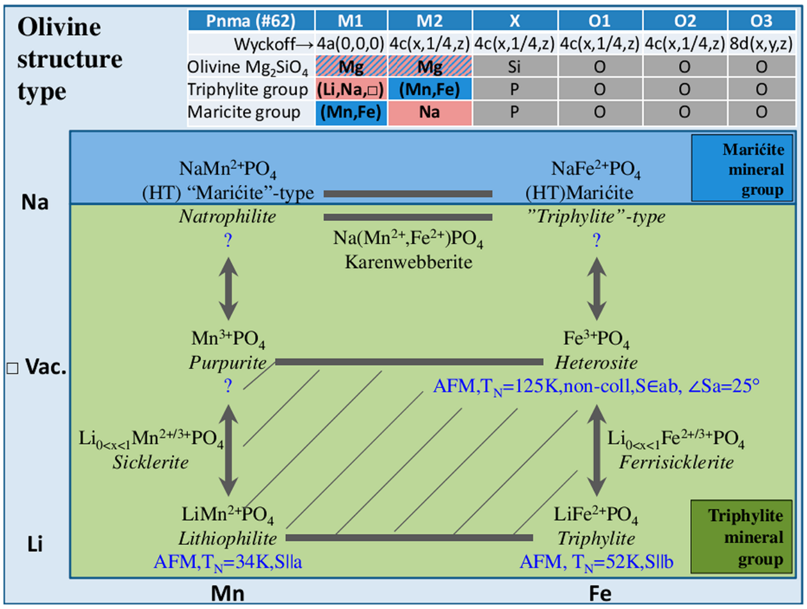

Pnma (#62)	M1	M2	X	O1	O2	O3
Wyckoff→	4a(0,0,0)	4c(x,1/4,z)	4c(x,1/4,z)	4c(x,1/4,z)	4c(x,1/4,z)	8d(x,y,z)
Olivine Mg_2SiO_4	Mg	Mg	Si	O	O	O
Triphylite group	(Li,Na,□)	(Mn,Fe)	P	O	O	O
Maricite group	(Mn,Fe)	Na	P	O	O	O

Figure 1. Crystal chemistry of the triphylite and maricite mineral groups. Minerals shown in italics are derived from lithiophilite and triphylite by low-temperature Li^+ leaching and substitution. Thick solid lines/arrows and hashed area show documented solid solution series between compositions. Text in blue shows information on magnetic structures.

transition metals (M) or are vacant in an ordered fashion. If transition metals reside in the $M2(4c)$ site and the $M1(4a)$ site is occupied by Li/Na or is vacant then the structure belongs to the triphylite mineral group. If the metal distribution is reversed, with transition metals residing in the $M1(4a)$ site and Na occupying the $M2(4c)$ site, the structure belongs to the maricite group. The crystal chemistry of various related minerals is summarized in Figure 1. As can be seen, the materials with the larger Na^+ cation are more stable in the maricite form, while the isostructural triphylite group compositions in Figure 1 are naturally derived from the triphylite $LiFePO_4$ or lithiophilite $LiMnPO_4$ by lithium leaching or sodium exchange at low temperature and are metastable. When heated, the products transform to thermodynamically stable modifications, e.g., heterosite-$FePO_4$ → α-berlinite-$FePO_4$,[35] triphylite-$NaFePO_4$ → maricite-$NaFePO_4$,[36] etc. As mentioned above, triphylite and maricite structure types have completely different connectivity of alkali metal sites. While the former allows Li or Na mobility and thus various chimie douce reactions depicted in Figure 1 with arrows, the latter has alkali metals trapped in the cavities which are not connected by suitable pathways resulting in much lower ionic conductivity.

Figure 1 also shows that while the magnetic structure and properties of lithium triphylite-type lithium phosphates were previously investigated, magnetic structures of the sodium analogues have not been studied so far. In the present work, we report the magnetic structure and properties of two $NaFePO_4$ polymorphs prepared by chimie douce and conventional high-temperature synthesis and compare the results with those previously reported for (triphylite) $LiFePO_4$.[37]

■ EXPERIMENTAL SECTION

Material Synthesis. The maricite $NaFePO_4$ phase was synthesized by a conventional solid-state method. A stoichiometric 1:2:2 molar mixture of Na_2CO_3 (Wako, 99%), $FeC_2O_4\cdot 2H_2O$ (Junsei, 99%), and $(NH_4)_2HPO_4$ (Wako, 99%) was prepared by wet planetary ball milling in acetone media for 1 h (600 rpm) using Cr-hardened stainless-steel (Cr-SS) milling media and container. Following, the acetone was dried, and the precursor mixture was ground, pressed into pellets, and sintered at 600 °C (heating rate = 10 °C/min) for 8 h in a tubular furnace under argon flow to obtain the desired phase.

Direct preparation of triphylite $NaFePO_4$ is cumbersome, being less favored thermodynamically. Thus, it was derived from triphylite $LiFePO_4$ instead. Triphylite $LiFePO_4$ was first prepared by the solid-state method (as described above) using a stoichiometric mixture of Li_2CO_3 (Wako, 99%), $FeC_2O_4\cdot 2H_2O$ (Junsei, 99%), and $(NH_4)_2HPO_4$ (Wako, 99%). The final product was obtained by annealing the precursor mixture at 650 °C for 8 h in steady Ar flow. Chemical oxidation was performed by adding a 1:1.5 molar mixture of $LiFePO_4$ and NO_2BF_4 (Alfa Aesar, 96%) to acetonitrile solvent (Wako, H_2O level < 5 ppm). This solution was stirred overnight (at 25 °C) under steady argon flow, and the resulting $FePO_4$ powder was filtered and dried. Afterward, chemical reduction and simultaneous sodiation was conducted using $FePO_4$ and NaI in acetonitrile medium with steady stirring for 48 h (at 60 °C) to ensure complete formation of triphylite $NaFePO_4$ phase. The chemical oxidation and reduction reactions can be written as

$$LiFePO_4 + NO_2BF_4 \rightarrow FePO_4 + LiBF_4 + NO_2 \uparrow \text{(delithiation)}$$

$$FePO_4 + \frac{3}{2}NaI \rightarrow NaFePO_4 + \frac{1}{2}NaI_3\text{(sodiation)}$$

The two distinct polymorphs of $NaFePO_4$ were used for various structural characterization as detailed below. For clarity, from here onward, the maricite and triphylite phases have been referred as m-$NaFePO_4$ and t-$NaFePO_4$, respectively.

Structural Analysis. X-ray powder diffraction patterns on $NaFePO_4$ polymorphs were obtained with a Bruker AXS D8 ADVANCE diffractometer (operating at 35 mA, 40 kV) equipped with a Co Kα source (λ_1 = 1.78897 Å, λ_2 = 1.7929 Å) and a Vantec-1 linear position-sensitive detector. The atmosphere-controlled high-temperature XRD analysis of t-$NaFePO_4$ sample was carried out with a Rigaku RINT-TTR III powder diffractometer (operating at 50 kV, 300 mA) equipped with a Cu Kα source (λ_1 = 1.54056 Å, λ_2 = 1.54439 Å). Under steady N_2 flow (100 cc/min), the sample was heated (from RT to 600 °C, at an interval of 100 °C) inside a Rigaku Reactor-X chamber with a beryllium window. After keeping the sample at target temperatures for 1 h, diffraction patterns were acquired. Typical scans were made in the 2θ range of 10−80° (step size of $0.03°\cdot s^{-1}$). Rietveld refinement was performed with a TOPAS V3.0 program, and the crystal structures were drawn using the VESTA software.[38]

Mössbauer Spectroscopy. Mössbauer spectra were collected with a Topologic System Inc. spectrometer equipped with a ^{57}Co γ-ray source (calibrated with an α-Fe standard) and analyzed with MossWinn3.0 software.

Magnetic Susceptibility and Specific Heat Analyses. Magnetic susceptibility and heat capacity measurements of the $NaFePO_4$ polymorphs were conducted with a Quantum Design PPMS instrument. Susceptibility was recorded in a zero-field-cooled mode with an applied field of 10 kOe in the temperature range of 2−300 K. Heat capacity measurements were performed on *m*-$NaFePO_4$ and *t*-$NaFePO_4$ pellets made of powder samples over the temperature range of 2−300 K.

Neutron Powder Diffraction. Neutron powder diffraction (NPD) patterns were collected on the high-resolution powder diffractometer Echidna at the OPAL facility (Lucas Height, Australia) using neutrons of wavelength 2.4395 Å. Approximately 2 g of powder sample was loaded in a 6 mm diameter cylindrical vanadium can, and diffraction patterns were collected between 300 and 3 K using a closed-cycle refrigerator. The magnetic structure was analyzed using the FullProf Suite[39] with the default neutron scattering lengths and Fe^{2+} magnetic form factor.

■ RESULTS AND DISCUSSION

Materials and Crystal Structures. As direct synthesis of electrochemically active *t*-$NaFePO_4$ phase is cumbersome, we adopted an indirect synthesis route. Single-phase $LiFePO_4$ was used as a precursor to conduct chemical delithiation (oxidation) followed by chemical sodiation (reduction) to obtain phase-pure *t*-$NaFePO_4$ (Figure 2). The striking structural similarity enabled efficient (topotactic) removal of Li and insertion of Na to obtain the *t*-$NaFePO_4$ polymorph. Comparative lattice parameters are summarized in Table 1. On the other hand, the thermodynamically stable *m*-$NaFePO_4$ polymorph was readily prepared by direct one-step synthesis. The $NaFePO_4$ system exhibits an irreversible phase transition from *t*-$NaFePO_4$ to *m*-$NaFePO_4$ around 480 °C as shown by variable-temperature X-ray diffraction patterns (Figure 3a).

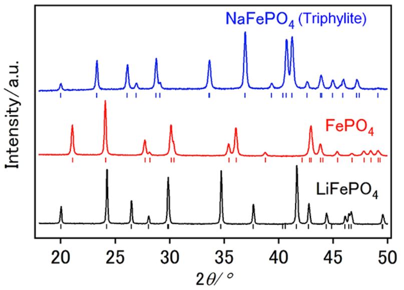

Figure 2. Comparative powder XRD patterns of triphylite $LiFePO_4$ starting material (black), chemically delithiated heterosite $FePO_4$ (red), and chemically sodiated triphylite $NaFePO_4$ end product (blue). Corresponding Braggs diffraction peaks are shown as tick marks.

Table 1. Lattice Parameters of $LiFePO_4$, $FePO_4$, and $NaFePO_4$ Products Based on the X-ray Powder Diffraction Data

materials	*a*/Å	*b*/Å	*c*/Å	*V*/Å^3
$LiFePO_4$ (triphylite)	10.3202(6)	6.0035(4)	4.6928(4)	291.020(8)
$FePO_4$ (heterosite)	9.8152(5)	5.7885(3)	4.7809(3)	271.593(4)
$NaFePO_4$ (triphylite)	10.4051(4)	6.2216(2)	4.9486(2)	319.933(9)
$NaFePO_4$ (maricite)	8.9773(3)	6.8679(2)	5.0434(2)	310.951(2)

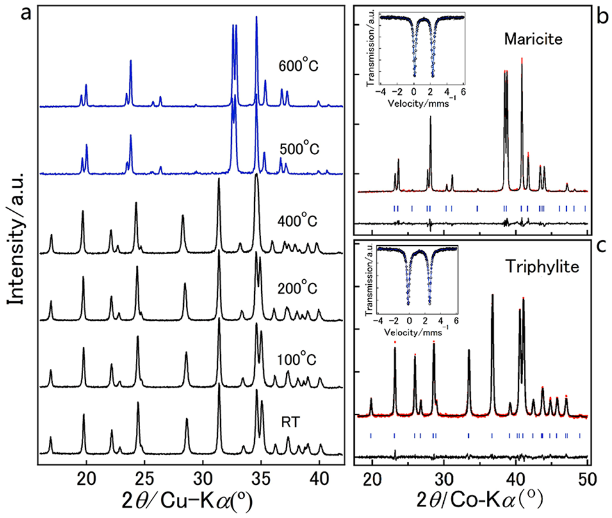

Figure 3. (a) High-temperature in situ X-ray diffraction patterns showing the triphylite to maricite phase transition (400 °C < T_t < 500 °C) in $NaFePO_4$ system. Triphylite phases at lower temperature (RT < T < 400 °C) and maricite phases at higher temperature (500 °C < T < 600 °C) are presented in black and blue, respectively. Rietveld refinement of *m*-$NaFePO_4$ (b) and *t*-$NaFePO_4$ (c) polymorphs are shown with the experimental data (red dots), simulated powder pattern (black line), Bragg diffraction positions (blue ticks), and difference between the experimental and theoretical patterns (black line). (Inset images) Corresponding Mössbauer spectra of $NaFePO_4$ polymorphs fitted with one Fe^{2+} doublet confirming the absence of any Fe^{3+} impurities.

Formation of high-purity $NaFePO_4$ polymorphs is confirmed by Rietveld refinement in Figure 3b and 3c. Mössbauer analysis further confirms the presence of Fe^{2+} species fitted with one doublet. Crystal structures of both these polymorphs, consisting slightly distorted FeO_6 octahedra and PO_4 tetrahedra units, are illustrated in Figure 4. The *t*-$NaFePO_4$ involves corner-sharing FeO_6 units, with edge sharing between neighboring FeO_6−PO_4. The electrostatic Coulombic repulsion between Fe^{2+} and P^{5+} leads to longer Fe−O bond lengths, which has a positive impact on realizing higher Fe^{3+}/Fe^{2+} redox potential. Similar to $LiFePO_4$, it offers a one-dimensional channel for Na^+ diffusion along the *b* direction, making it suitable as a cathode candidate. In the contrary, the *m*-$NaFePO_4$ has edge-sharing FeO_6−FeO_6 units, which are tied by neighboring PO_4 units in corner-sharing fashion, offering no cationic channels for Na^+ movement. The signature difference between these two polymorphs is the corner-sharing and edge-sharing FeO_6 chains for triphylite and maricite cases, respectively, as highlighted in Figure 4c. The local geometry (Fe−O−Fe bond angle) accounts for the significant influence in local spin−spin exchange interaction, physical properties, and overall magnetic structures as described in the following sections.

Magnetic Susceptibility and Specific Heat of *m*-$NaFePO_4$ and *t*-$NaFePO_4$. The results of magnetic property measurements for the two polymorphs are presented in Figure 5. Magnetic susceptibility χ as a function of temperature

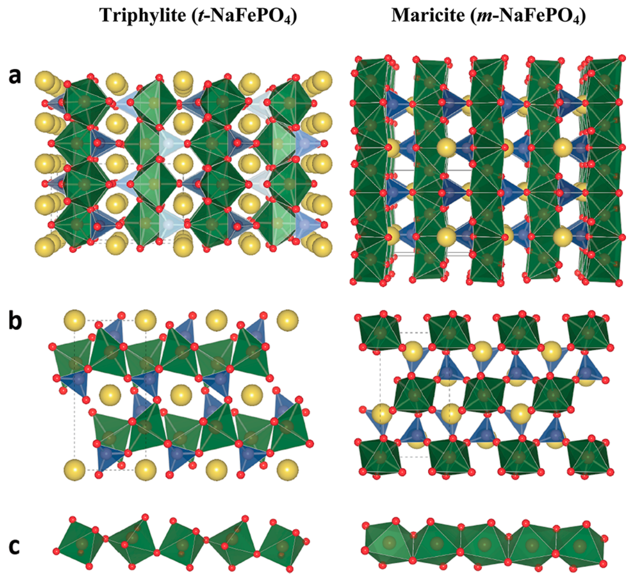

Figure 4. Schematic presentation of orthorhombic structured triphylite $NaFePO_4$ (left) and maricite $NaFePO_4$ (right) polymorphs (a and b). FeO_6 octahedra (green), PO_4 tetrahedra (blue), and Na atoms (yellow) are depicted. (c) Corner-sharing and edge-sharing coordinations among chains of neighboring FeO_6 octahedra are highlighted for triphylite and maricite phases, respectively.

revealed a signature of magnetic transitions at ~50 and ~13 K for *t*-$NaFePO_4$ and *m*-$NaFePO_4$, respectively.

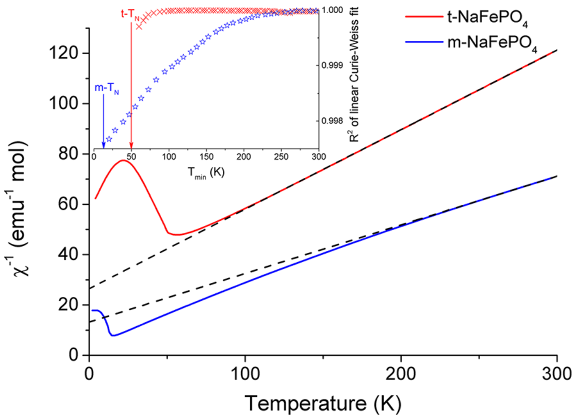

Figure 5. Inverse magnetic susceptibility (χ^{-1}) as a function of temperature for *t*-$NaFePO_4$ (red) and *m*-$NaFePO_4$ (blue) measured with the applied field of H = 10 kOe. The dashed lines show the results of data analysis with the Curie-Weiss law. (Inset) R^2 for a linear fit of the χ^{-1} vs T data as a function of the lower limit T_{min} of the fitted range T_{min}−300 K. See text for details.

The corresponding χ^{-1} vs T for *t*-$NaFePO_4$ demonstrates linear Curie−Weiss behavior above the transition temperature. A linear fit in the range 100−300 K yielded $\Theta = -84$ K and an effective moment of 5.0 μB. These values are very close to those reported for the parent $LiFePO_4$ (see ref 27 and references therein), which suggests that magnetic interactions in the $[FePO_4]^-$ framework are practically unaffected by substitution of Na^+ for Li^+. The similarity between the bulk magnetic structure of *t*-$NaFePO_4$ and that of the parent $LiFePO_4$ is further discussed below.

In contrast, the inverse susceptibility of *m*-$NaFePO_4$ as a function of temperature is clearly nonlinear above the transition (Figure 5). This can be interpreted assuming a substantial temperature-independent paramagnetic contribution or, more likely, is a result of short-range correlations persisting above T_N. Analysis of the magnetic structure discussed below strongly points to the latter scenario. The non-Curie−Weiss behavior of the *m*-$NaFePO_4$ magnetic susceptibility data can be especially clearly seen in Figure 5 (inset), showing the R^2 for a linear fit of the χ^{-1} vs T data as a function of the lower limit T_{min} of the fitted range T_{min}−300 K. While χ^{-1} vs T for *t*-$NaFePO_4$ becomes linear at ~80 K, i.e., only 30 K above the $T_N \approx 50$ K, for *m*-$NaFePO_4$ it occurs only above ~240 K, i.e., ~230 K above $T_N \approx 13$ K. A linear fit in the range 240−300 K yielded $\Theta = -83$ K and an effective moment of 6.4 μB. As for *t*-$NaFePO_4$, the effective magnetic moment of *m*-$NaFePO_4$ is larger than the spin-only value for $S = 2$ Fe^{2+}, which points to incomplete quenching of the orbital moment, as is common in Fe^{2+} compounds (see ref 27 and references therein). At the same time, the value of the frustration index[40] $f = |\Theta|/T_N \approx 6.4$ suggests that *m*-$NaFePO_4$ is a moderately magnetically frustrated material which nevertheless undergoes long-range magnetic ordering as is also confirmed by characteristic λ-type anomalies observed in the complementary specific heat data collected for both polymorphs (Figure 6).

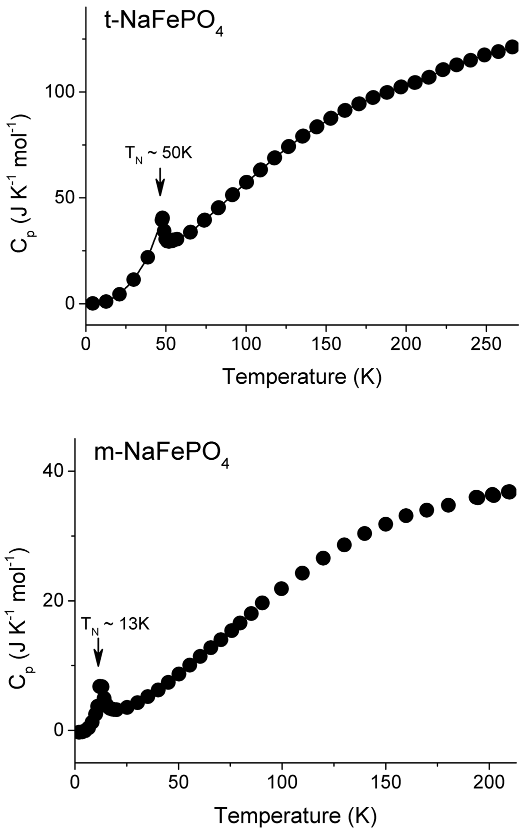

Figure 6. Specific heat as a function of temperature for *t*-$NaFePO_4$ (top) and *m*-$NaFePO_4$ (bottom).

In order to estimate the magnetic entropy release associated with ordering, the lattice and magnetic components of the total heat capacity were to be separated first. Since no heat capacity data are available for nonmagnetic analogues of the $NaFePO_4$ polymorphs, we estimated the lattice contribution using the Debye model

$$c_{p,\text{phon}}(T,\,\theta_{\text{D}}) = 9R\left(\frac{T}{\theta_{\text{D}}}\right)^3 \int_0^{\theta_{\text{D}}/T} \frac{x^4 e^x}{(e^x - 1)^2}\text{d}x$$

where R is the gas constant and θ_{D} is the Debye temperature. Furthermore, to account for the significant difference in atomic masses of the elements constituting the compositions (i.e., O vs Fe), experimental data were analyzed using a model with two phonon spectra

$$c_{p,\text{phon}} = n\cdot c_{p,\text{phon},1}(T,\,\Theta_{\text{D},1}) + (7-n)\cdot c_{p,\text{phon},2}(T,\,\Theta_{\text{D},2})$$

The fit (Figure S1, Supporting Information) to the high-temperature range of the experimental data for *t*-NaFePO$_4$ ($T > 100$ K) yielded n, $\theta_{\text{D},1}$, and $\theta_{\text{D},2}$ equal to 3.7, 1038, and 318 K, which is consistent with the lighter element sublattice (4 O atoms) having the higher Debye temperature. Although the magnetic entropy ($S_{\text{mag}} = \int_0^T (C_{p,\text{mag}})/T\,\text{d}T$) reaches the value ~10 J mol^{-1} K^{-1}, lower than the theoretical $R\ln(2S+1) = 13.4$ J mol^{-1} K^{-1} expected for $S = 2$ Fe^{2+}, which probably indicates a systematic error in the procedure of estimating lattice contribution, what is more important is the observation that magnetic entropy reaches the saturated value by ~80 K, i.e., at temperatures close to the transition ($T_{\text{N}} \approx 50$ K), in agreement with the susceptibility data (Figure 5, inset) and in contrast to *m*-NaFePO$_4$.

Unfortunately, our attempts to perform the same analysis of heat capacity data for *m*-NaFePO$_4$ failed as the temperature range of the truly paramagnetic state, i.e., between $T \gtrsim 240$ K (Figure 5, inset) and the upper limit of our data, 300 K, proved to be too narrow to obtain a stable fit with the Debye equation. Further experiments in the temperature range extending above room temperature would be needed to assess the behavior of the magnetic entropy for the maricite phase.

Crystal and Magnetic Structure of *t*-NaFePO$_4$ from the NPD Data. Rietveld analysis of NPD data collected at 300 K yielded results in very good agreement with those previously reported for *t*-NaFePO$_4$ based on X-ray powder diffraction.[36] The final Rietveld plot and crystallographic information are presented in Figure 7 and Table 2. As can be seen from the table, the bond valence sums[41] deviate from the expected formal oxidation states by less than 10% for all atoms except sodium. The fact that Na$^+$ is overbonded by ~40% is not surprising, as after intercalation it occupies the sites originally formed in the triphylite structure for much smaller Li$^+$. For comparison, the BVS calculated for Li$^+$ in the parent LiFePO$_4$ based on the previously reported crystal structure refined against NPD data,[37] 0.96, is much closer to the expected formal oxidation state.

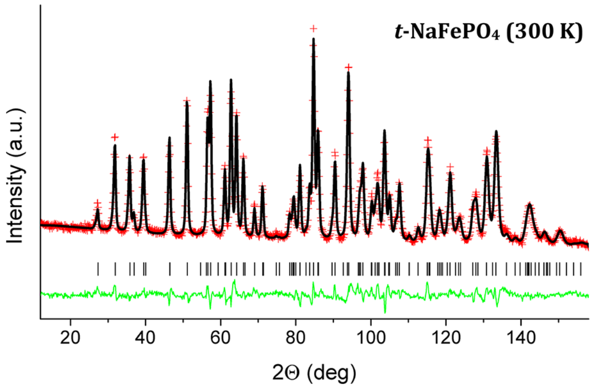

Figure 7. Rietveld plot for the *t*-NaFePO$_4$ neutron powder diffraction data collected at 300 K. Red crosses and black and green solid lines indicate the observed and calculated patterns and their difference, respectively. Tick marks indicate the position of the diffraction peaks. $R_{\text{p}} = 3.25\%$, $R_{\text{wp}} = 4.19\%$, $R_{\text{Bragg}} = 4.18\%$, $\chi^2 = 4.40$.

Examination of the neutron diffraction patterns collected between 3 and 55 K revealed additional intensity due to magnetic ordering developing below 50 K (Figure 8). This is consistent with the magnetic susceptibility and heat capacity data which suggested an antiferromagnetic transition at ~50 K (Figures 5 and 6). All diffraction peaks of *t*-NaFePO$_4$ with magnetic contributions could be indexed in the crystallographic unit cell, i.e., with the propagation vector $k = (0,0,0)$ (Figure 9, Table 3). For the 4c(x, 0.75, z) Wyckoff site of the *Pnma* space group, the magnetic representation decomposes in terms of eight one-dimensional irreducible representations (IR) as $\Gamma_{\text{mag}}(4\text{c}) = \Gamma1 + 2\Gamma2 + 2\Gamma3 + \Gamma4 + \Gamma5 + 2\Gamma6 + 2\Gamma7 + \Gamma8$. The associated basis vectors are listed in Table S1, Supporting Information. The best agreement between the experimental and the calculated powder diffraction patterns was obtained for the Γ4 representation (equivalent to the *Pnma′* Shubnikov group, Opechowski-Guccione #62.5.506), which means that the magnetic structure of *t*-NaFePO$_4$ is qualitatively the same as that previously reported for LiFePO$_4$ based on NPD data.[21,37] We note that in a later report of a single-crystal neutron scattering study of LiFePO$_4$ it was observed that the magnetic moments are not strictly parallel to the *b* axis.[26] We did not find any experimental evidence of magnetic moment titling from the *b* axis in our NPD data for *t*-NaFePO$_4$, although we cannot completely rule out such possibility as powder diffraction data may not be sensitive enough to detect the small angles which were estimated to be 3.0(5)° and 7.5(5)° toward the *c* and *a* axes, respectively.[26] The magnetic structure model is also consistent with the magnetic measurement data, which showed that T_{N} was not affected by Na−Li exchange in the triphylite framework. Apparently the distortion of the crystal structure which occurs due to substitution on Li$^+$ by Na$^+$ is too small to modify the magnetic interactions (previously discussed in detail[37]) and the magnetic structure adopts the same type. The magnetic moment value determined from the NPD data collected at 3 K, 4.55(5) μ_{B}, is significantly higher than expected for Fe^{2+} ($S = 2$), which strongly points to a contribution from a partially unquenched orbital moment. This is in agreement with the magnetic susceptibility data and was previously also conjectured for LiFePO$_4$ based on the NPD determined moment value, 4.19(5) μ_{B}.[37]

The magnetic structure of *t*-NaFePO$_4$ can be rationalized by considering it as a stacking of [FeO$_{6/2}$] octahedral layers perpendicular to the *a* axis (Figure 10). Corner sharing within layers, in combination with the Fe−O−Fe angles ~131°, result in antiferromagnetic superexchange as expected from the Goodenough−Kanamori rules (Figure 10b).[42−44] The layers are linked by tetrahedral phosphate PO$_4$ groups, and the supersuperexchange interactions via Fe−O···O−Fe contacts with Fe−O···O/O···O−Fe angles ~125°/145° then result in antiferromagnetic interlayer coupling (Figure 10c).

Crystal and Magnetic Structure of *m*-NaFePO$_4$ from the NPD Data. The results of analysis of the NPD data collected for *m*-NaFePO$_4$ at 300 K agree very well with the previous X-ray diffraction study.[17] The final Rietveld plot and crystallographic information are presented in Figure 11 and Table 4. In contrast to the metastable *t*-NaFePO$_4$, the bond-

Table 2. Crystal Structural Parameters for *t*-$NaFePO_4$ Based on the Rietveld Refinement Against NPD Data Collected at 300 K[a]

atom	Wyckoff site	*x*	*y*	*z*	B_{iso}, Å^2	BVS
Na	4a	0	0	0	1.7(2)	1.41(1)
P	4c	0.1079(5)	0.75	0.4429(11)	1.08(16)	4.96(4)
Fe	4c	0.2878(3)	0.75	0.9842(7)	0.83(11)	1.83(1)
O1	4c	0.1129(5)	0.75	0.7546(12)	0.73(14)	2.07(3)
O2	4c	0.4681(5)	0.75	0.1589(10)	0.99(18)	2.15(3)
O3	8d	0.1749(5)	0.9435(5)	0.3114(6)	1.12(11)	1.99(2)

[a] Space group *Pnma* (No. 62), $a = 10.4014(3)$ Å, $b = 6.21836(16)$ Å, $c = 4.94631(13)$ Å, $V = 319.924(19)$ Å^3.

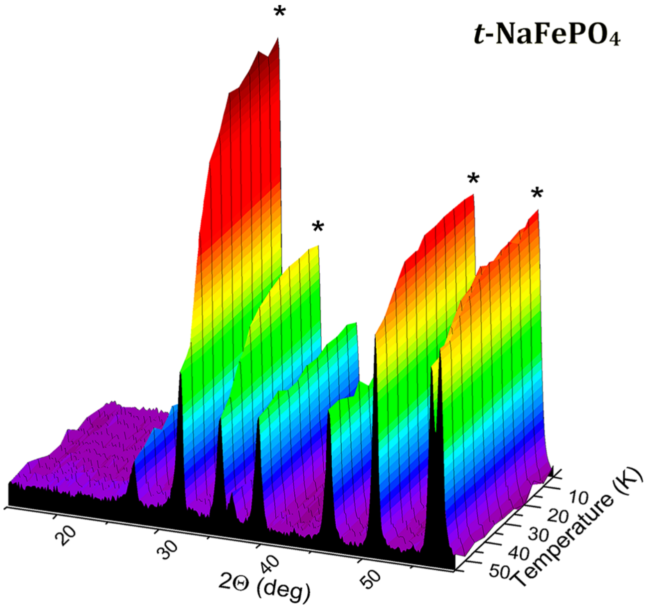

Figure 8. Evolution of neutron powder diffraction data as a function of temperature for *t*-$NaFePO_4$ between 55 and 3 K. Asterisks indicate the peaks with magnetic scattering contribution increasing upon cooling to low temperature.

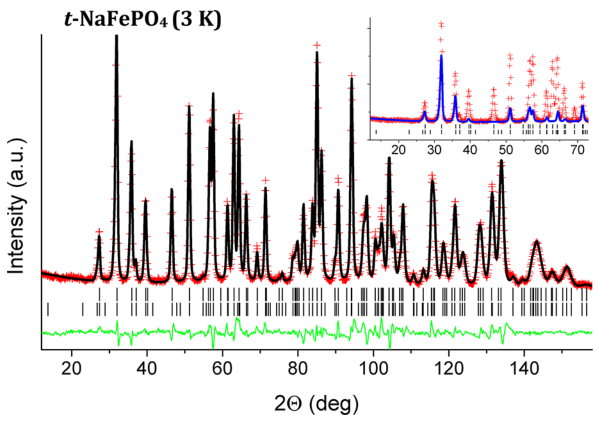

Figure 9. Rietveld plot for the *t*-$NaFePO_4$ NPD data at 3 K. Red crosses and black and green solid lines indicate the observed and calculated patterns and their difference, respectively. Two rows of black tick marks indicate position of the nuclear (top) and magnetic (bottom) diffraction peaks. Blue curve in the inset shows magnetic contribution. $R_p = 3.11\%$, $R_{wp} = 4.18\%$, $\chi^2 = 8.9$, $R_{mag} = 4.35\%$.

Table 3. Crystal Structural Parameters for *t*-$NaFePO_4$ Based on the Rietveld Refinement Against NPD Data Collected at 3 K[a]

atom	Wyckoff site	*x*	*y*	*z*	B_{iso}, Å^2
Na	4a	0	0	0	0.37(6)
P	4c	0.1078(4)	0.75	0.4419(9)	0.37(6)
Fe	4c	0.2875(3)	0.75	0.9853(6)	0.37(6)
O1	4c	0.1114(4)	0.75	0.7543(9)	0.37(6)
O2	4c	0.4664(4)	0.75	0.1623(8)	0.37(6)
O3	8d	0.1753(5)	0.9433(5)	0.3102(5)	0.37(6)

[a] Space group *Pnma* (No. 62), $a = 10.3936(2)$ Å, $b = 6.19768\ (13)$ Å, $c = 4.93567(10)$ Å, $V = 317.939(12)$ Å^3.

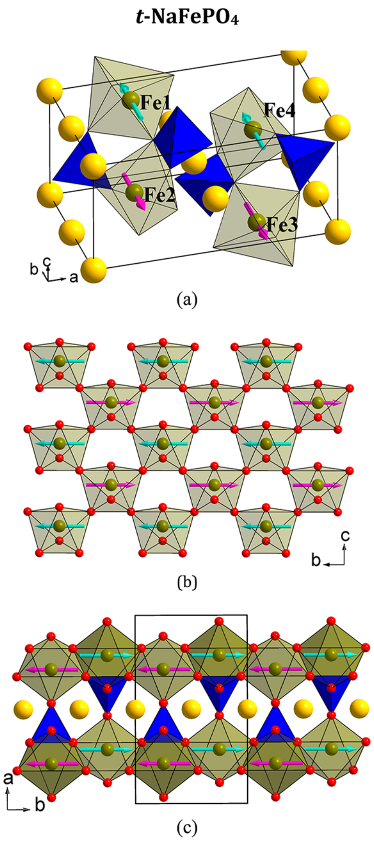

Figure 10. (a) General view of the crystal and magnetic structure of *t*-$NaFePO_4$ with labels showing the numbering scheme of Table S1, Supporting Information, (b) view of a single antiferromagnetically ordered layer of corner-sharing [FeO_6] octahedra, and (c) view along the *c* axis showing connection of layers via phosphate groups.

valence sum for Na^+ in *m*-$NaFePO_4$, 1.08, is very close to the expected formal oxidation state (Table 4).

Comparison of the NPD data collected at 3 and 20 K, i.e., below and above the transition observed in the magnetic susceptibility and heat capacity data (Figures 5 and 6), clearly revealed additional diffraction intensity due to long-range magnetic ordering. All diffraction peaks of *m*-$NaFePO_4$ with magnetic contributions could be indexed with the propagation

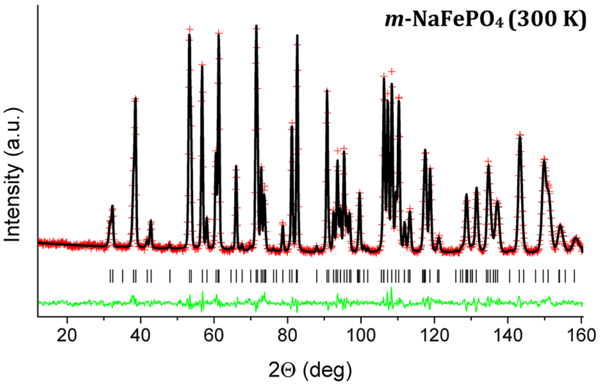

Figure 11. Rietveld plot for the *m*-$NaFePO_4$ neutron powder diffraction data collected at 300 K. Red crosses and black and green solid lines indicate the observed and calculated patterns and their difference, respectively. Tick marks indicate the position of the diffraction peaks. R_p = 3.51%, R_{wp} = 4.58%, R_{Bragg} = 2.55%, χ^2 = 2.04.

vector k = (1/2,0,1/2). Representational analysis was carried out the same way as for *t*-$NaFePO_4$. For the 4a(0,0,0) Wyckoff site of the *Pnma* space group, the magnetic representation decomposes in terms of four one-dimensional irreducible representations as $\Gamma_{mag}(4a) = 3\Gamma1 + 3\Gamma3 + 3\Gamma5 + 3\Gamma7$. The associated basis vectors are listed in Table S2, Supporting Information. All IRs are complex with Herring coefficient 0 and thus do not have Shubnikov group equivalents. To obtain real basis vectors, the complex conjugate IRs were combined as $\Gamma1 + \Gamma5$ and $\Gamma3 + \Gamma7$. Only the latter combination resulted in good agreement between the experimental and the calculated diffraction patterns. Although by symmetry the pairs Fe1/Fe3 and Fe2/Fe4 can carry different magnetic moments, we assumed equal moment values on all the sites, i.e., a so-called constant moment model. Finally, examination of the diffraction data showed no evidence of the scattering corresponding to a magnetic moment component along the *b* axis, and therefore, only the parameters defining the moment in the *ac* plane were refined. The final Rietveld plot and crystallographic information are presented in Figure 12 and Table 5, respectively. The resulting magnetic structure, which can also be described by the $P_{2c}2_1/m'$ Shubnikov group (#11.7.65) with a magnetic monoclinic cell related to the chemical orthorhombic cell as (*a*-*c*,*b*,2*c*), is illustrated in Figure 13. The components of the magnetic moment along the *a* and *c* axes are 2.59(3) and 2.90(4) μ_B, respectively, yielding the total moment of 3.89(3) μ_B. Along the *c* axis the moments are collinear with the angle between the moment and the *a* axis in the *ac* plane being 41.8(5)°, which results in the moment of the neighbor in the (101) direction being almost perpendicular, 84(1)° (Figure 13c).

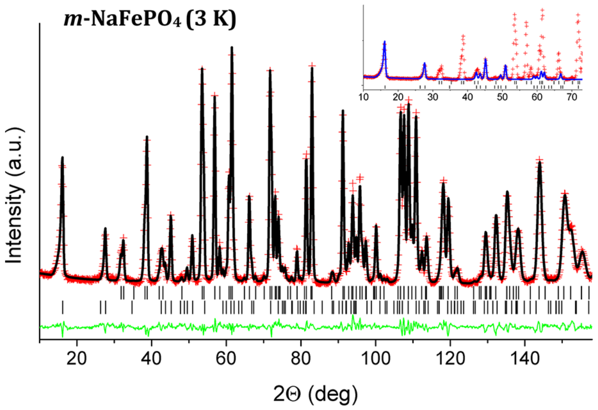

Figure 12. Rietveld plot for the *m*-$NaFePO_4$ NPD data at 3 K. Red crosses and black and green solid lines indicate the observed and calculated patterns and their difference, respectively. Two rows of black tick marks indicate position of the nuclear (top) and magnetic (bottom) diffraction peaks. Blue curve in the inset shows magnetic contribution. R_p = 3.72%, R_{wp} = 4.76%, χ^2 = 3.51, R_{mag} = 4.29%.

Table 5. Crystal Structural Parameters for *m*-$NaFePO_4$ Based on the Rietveld Refinement Against NPD Data Collected at 3 K[a]

atom	Wyckoff site	*x*	*y*	*z*	B_{iso}, Å^2
Fe	4a	0	0	0	0.10(3)
P	4c	0.1760(3)	0.25	0.4635(7)	0.10(3)
Na	4c	0.3492(5)	0.25	0.9726(10)	0.10(3)
O1	8c	0.1205(5)	0.0665(3)	0.3204(4)	0.10(3)
O2	4c	0.3493(3)	0.25	0.4590(6)	0.10(3)
O3	4c	0.1151(5)	0.25	0.7549(6)	0.10(3)

[a] Space group *Pnma* (No. 62), *a* = 8.96278(9) Å, *b* = 6.84285(11) Å, *c* = 5.02827(7) Å, *V* = 308.389(7) Å^3.

The magnetic structure can also be rationalized based on the Goodenough–Kanamori rules.[42−44] The nearest neighbors of a given Fe^{2+} d^6 cation are located at *b*/2–3.4 Å within rutile-type chains of trans-edge-sharing octahedra (Figure 13b) and interactions via Fe–O–Fe angles ≈ 94–103° approach the "90°"-regime favoring weak ferromagnetic coupling. At the same time, Fe–O···O–Fe supersuperexchange paths via phosphate groups promote antiferromagnetic interchain coupling. Closer examination of the chain arrangement in the structure reveals that they form an almost ideal triangular pattern (Figure 13c) with the monoclinic angle of the magnetic cell, 119.3°, being close to an ideal 120° value. In the case of the ideal ratio of the orthorhombic cell parameters $a/c = \sqrt{3}$, the system might have been completely geometrically frustrated without developing long-range magnetic order. The slight

Table 4. Crystal Structural Parameters for *m*-$NaFePO_4$ Based on the Rietveld Refinement Against NPD Data Collected at 300 K[a]

atom	Wyckoff site	*x*	*y*	*z*	B_{iso}, Å^2	BVS
Fe	4a	0	0	0	0.45(6)	1.92(1)
P	4c	0.1764(4)	0.25	0.4617(8)	0.44(9)	4.97(3)
Na	4c	0.3503(6)	0.25	0.9713(12)	1.08(11)	1.08(1)
O1	8c	0.1207(3)	0.0684(3)	0.3176(4)	0.73(6)	2.01(1)
O2	4c	0.3480(3)	0.25	0.4588(7)	0.62(8)	2.09(2)
O3	4c	0.1167(5)	0.25	0.7504(6)	0.34(7)	1.87(2)

[a] Space group *Pnma* (No. 62), *a* = 8.97639(11) Å, *b* = 6.86842(12) Å, *c* = 5.04292(7) Å, *V* = 310.914(8) Å^3.

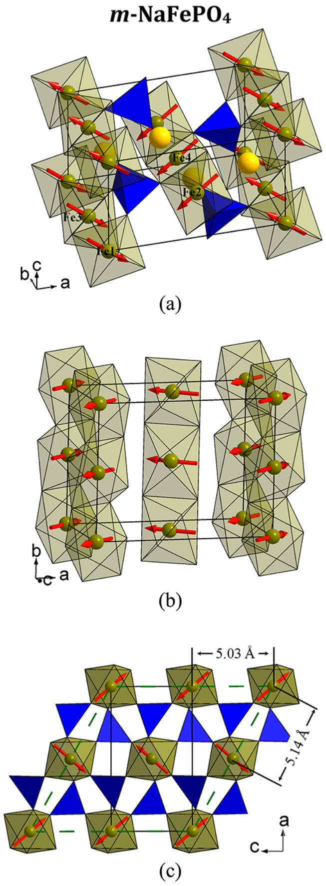

Figure 13. General view of the crystal and magnetic structure of *m*-$NaFePO_4$ (a), view of ferromagnetic rutile-type (FeO_6)-octahedral chains running along the *b* axis (b), and view along the *b* axis showing connection of octahedral chains via phosphate groups (c). Dashed line in c shows the magnetic monoclinic cell with respect to the chemical cell (solid line).

orthorhombic distortion resulting in nonequal Fe−Fe distances between rutile chains in the (001) and (101) directions (5.03 and 5.14 Å, respectively) lifts frustration, but the transition temperature remains low (13 K) compared to that of *t*-$NaFePO_4$ (50 K). The fragility of the magnetic structure can also explain the lower moment value found in *m*-$NaFePO_4$ compared to that of *t*-$NaFePO_4$, 3.89 and 4.57 μ_B, respectively.

CONCLUSIONS

In summary, we explored the magnetic structure and properties of the triphylite and maricite polymorphs of the sodium-ion battery cathode material $NaFePO_4$. Both modifications undergo antiferromagnetic transitions around 50 and 13 K, respectively. Neutron powder diffraction data analysis revealed that *t*-$NaFePO_4$ prepared by chimie douce from $LiFePO_4$ has the same magnetic structure as the parent material, i.e., antiferromagnetically ordered corrugated layers of corner-sharing (FeO_6) octahedra coupled antiferromagnetically by interlayer supersuperexchange via phosphate groups. In contrast, the maricite modification featuring the rutile-type chains of trans-edge sharing FeO_6 octahedra are ordered ferromagnetically within each chain with the moments confined to the *ac* plane. The chains are coupled antiferromagnetically, although the quasi one-dimensional character of the magnetic structure and the arrangement of the chains in a nearly ideal triangular pattern significantly lowers the temperature of magnetic transition.

ASSOCIATED CONTENT

Ⓢ Supporting Information

Tables enlisting the Basis vectors for triphylite and maricite polymorphs of $NaFePO_4$ and specific heat curve for *t*-$NaFePO_4$. This material is available free of charge via the Internet at http://pubs.acs.org.

AUTHOR INFORMATION

Corresponding Author

*Phone: +81-3-5841-7295. Fax: +81-3-5841-7488. E-mail: prabeer@chemsys.t.u-tokyo.ac.jp.

Notes

The authors declare no competing financial interest.

ACKNOWLEDGMENTS

We gratefully acknowledge financial support from Mitsubishi Motors Corp. and the Ministry of Education, Culture, Sports, Science and Technology, Japan (MEXT) under the 'Element Strategy Initiative for Catalysts & Batteries' (ESICB) project. P.B. is thankful to the Japan Society for the Promotion of Sciences for a JSPS Fellowship at the University of Tokyo. C.D.L. acknowledges the financial support by the Australian Research Council (DP110102662).

REFERENCES

(1) Whittingham, M. S. *Chem. Rev.* **2004**, *104*, 4271−4302.

(2) Etacheri, V.; Marom, R.; Elazari, R.; Salitra, G.; Aurbach, D. *Energy Environ. Sci.* **2011**, *4*, 3243−3262.

(3) Desilvestro, J.; Haas, O. *J. Electrochem. Soc.* **1990**, *137*, 5C−22C.

(4) Gong, Z.; Yang, Y. *Energy Environ. Sci.* **2011**, *4*, 3223−3242.

(5) Delmas, C.; Braconnier, J.-J.; Fouassier, C.; Hagenmuller, P. *Solid State Ionics* **1981**, 3−4, 165−169.

(6) Komaba, S.; Takei, C.; Nakayama, T.; Ogata, A.; Yabuuchi, N. *Electrochem. Commun.* **2010**, *12*, 355−358.

(7) Yabuuchi, N.; Kajiyama, M.; Iwatate, J.; Nishikawa, H.; Hitomi, S.; Okuyama, R.; Usui, R.; Yamada, Y.; Komaba, S. *Nat. Mater.* **2012**, *11*, 512−517.

(8) Ellis, B.; Makahnouk, W.; Makimura, Y.; Toghill, K.; Nazar, L. *Nat. Mater.* **2007**, *6*, 749−753.

(9) Barpanda, P.; Chotard, J. N.; Recham, N.; Delacourt, C.; Ati, M.; Dupont, L.; Armand, M.; Tarascon, J. M. *Inorg. Chem.* **2010**, *49*, 7401−7413.

(10) Kim, H.; Park, I.; Seo, D.-H.; Lee, S.; Kim, S.-W.; Kwon, W. J.; Park, Y.-U.; Kim, C. S.; Jeon, S.; Kang, K. *J. Am. Chem. Soc.* **2012**, *134*, 10369−10372.

(11) Barpanda, P.; Ye, T.; Nishimura, S.-i.; Chung, S.-C.; Yamada, Y.; Okubo, M.; Zhou, H.; Yamada, A. *Electrochem. Commun.* **2012**, *24*, 116−119.

(12) Barpanda, P.; Nishimura, S.; Yamada, A. *Adv. Energy Mater.* **2012**, *2*, 841−859.

(13) Palomares, V.; Serras, P.; Villaluenga, I.; Hueso, K. B.; Carretero-Gonzalez, J.; Rojo, T. *Energy Environ. Sci.* **2012**, *5*, 5884−5901.

(14) Padhi, A. K.; Nanjundaswamy, K. S.; Goodenough, J. B. *J. Electrochem. Soc.* **1997**, *144*, 1188−1194.

(15) Yamada, A.; Chung, S.-C.; Hinokuma, K. *J. Electrochem. Soc.* **2001**, *148*, A224−A229.

(16) Yamada, A.; Chung, S.-C. *J. Electrochem. Soc.* **2001**, *148*, A960−A967.

(17) Bridson, J. N.; Quinlan, S. E.; Tremaine, P. R. *Chem. Mater.* **1998**, *10*, 763−768.

(18) Ong, S. P.; Chevrier, V. L.; Hautier, G.; Jain, A.; Moore, C.; Kim, S.; Ma, X.; Ceder, G. *Energy Environ. Sci.* **2011**, *4*, 3680−3688.

(19) Oh, S.-M.; Myung, S.-T.; Hassoun, J.; Scrosati, B.; Sun, Y.-K. *Electrochem. Commun.* **2012**, *22*, 149−152.

(20) Casas-Cabanas, M.; Roddatis, V.; Saurel, D.; Kubiak, P.; Carretero-González, J.; Palomares, V.; Serras, P.; Rojo, T. *J. Mater. Chem.* **2012**, *22*, 17421−17423.

(21) Santoro, R. P.; Newnham, R. E. *Acta Crystallogr.* **1967**, *22*, 344−347.

(22) Santoro, R. P.; Segal, D. J.; Newnham, R. E. *J. Phys. Chem. Solids* **1966**, *27*, 1192−1193.

(23) Newnham, R. E.; Santoro, R. P.; Redman, M. J. *J. Phys. Chem. Solids* **1965**, *26*, 445−447.

(24) Vaknin, D.; Zarestky, J. L.; Ostenson, J. E.; Chakoumakos, B. C.; Goñi, A.; Pagliuso, P. J.; Rojo, T.; Barberis, G. E. *Phys. Rev. B* **1999**, *60*, 1100−1110.

(25) Vaknin, D.; Zarestky, J. L.; Miller, L. L.; Rivera, J. P.; Schmid, H. *Phys. Rev. B* **2002**, *65*, 224414.

(26) Li, J.; Garlea, V. O.; Zarestky, J. L.; Vaknin, D. *Phys. Rev. B* **2006**, *73*, 024410.

(27) Liang, G.; Park, K.; Li, J.; Benson, R. E.; Vaknin, D.; Markert, J. T.; Croft, M. C. *Phys. Rev. B* **2008**, *77*, 064414.

(28) Li, J.; Tian, W.; Chen, Y.; Zarestky, J. L.; Lynn, J. W.; Vaknin, D. *Phys. Rev. B* **2009**, *79*, 144410.

(29) Kornev, I.; Bichurin, M.; Rivera, J. P.; Gentil, S.; Schmid, H.; Jansen, A. G. M.; Wyder, P. *Phys. Rev. B* **2000**, *62*, 12247−12253.

(30) Jensen, T. B. S.; Christensen, N. B.; Kenzelmann, M.; Rønnow, H. M.; Niedermayer, C.; Andersen, N. H.; Lefmann, K.; Schefer, J.; v. Zimmermann, M.; Li, J.; Zarestky, J. L.; Vaknin, D. *Phys. Rev. B* **2009**, *79*, 092412.

(31) Tian, W.; Li, J.; Li, H.; Lynn, J. W.; Zarestky, J. L.; Vaknin, D. *J. Phys. Conf. Ser.* **2010**, *251*, 012005.

(32) Kharchenko, N. F.; Khrustalev, V. M.; Savitskii, V. N. *Low Temp. Phys.* **2010**, *36*, 558−564.

(33) Toft-Petersen, R.; Jensen, J.; Jensen, T. B. S.; Andersen, N. H.; Christensen, N. B.; Niedermayer, C.; Kenzelmann, M.; Skoulatos, M.; Le, M. D.; Lefmann, K.; Hansen, S. R.; Li, J.; Zarestky, J. L.; Vaknin, D. *Phys. Rev. B* **2011**, *84*, 054408.

(34) Toft-Petersen, R.; Andersen, N. H.; Li, H.; Li, J.; Tian, W.; Bud'ko, S. L.; Jensen, T. B. S.; Niedermayer, C.; Laver, M.; Zaharko, O.; Lynn, J. W.; Vaknin, D. *Phys. Rev. B* **2012**, *85*, 224415.

(35) Iyer, R. G.; Delacourt, C.; Masquelier, C.; Tarascon, J.-M.; Navrotsky, A. *Electrochem. Solid-State Lett.* **2006**, *9*, A46−A48.

(36) Moreau, P.; Guyomard, D.; Gaubicher, J.; Boucher, F. *Chem. Mater.* **2010**, *22*, 4126−4128.

(37) Rousse, G.; Rodriguez-Carvajal, J.; Patoux, S.; Masquelier, C. *Chem. Mater.* **2003**, *15*, 4082−4090.

(38) Momma, K.; Izumi, F.; Appl., J. *Crystallogr* **2011**, *44*, 1272−1276.

(39) Rodríguez-Carvajal, J. *Physica B: Physica B: Condensed Matter* **1993**, *192*, 55−69.

(40) Ramirez, A. *Annu. Rev. Mater. Sci.* **1994**, *24*, 453−480.

(41) Brown, I. D.; Altermatt, D. *Acta Crystallogr. B* **1985**, *41*, 244−247.

(42) Goodenough, J. B. *Magnetism and the chemical bond*; Interscience Publishers: New York, 1963; Vol. *1*.

(43) Goodenough, J. B. *Phys. Rev.* **1960**, *117*, 1442−1451.

(44) Kanamori, J. *J. Phys. Chem. Solids* **1959**, *10*, 87−98.